

# Mass Selection Bias in Galaxy Cluster Peculiar Velocities from the Kinetic Sunyaev–Zel’dovich Effect

Alan C. Peel<sup>1</sup>\*

<sup>1</sup>Department of Applied Mathematics and Theoretical Physics, University of Cambridge, Cambridge CB3 0WA, United Kingdom

submitted to MNRAS

## ABSTRACT

Upcoming surveys for galaxy clusters using the Sunyaev–Zel’dovich effect are potentially sensitive enough to create a peculiar velocity catalog. The statistics of these peculiar velocities are sensitive to cosmological parameters. We develop a method to explore parameter space using N-body simulations in order to quantify dark matter halo velocity statistics which will be useful for cluster peculiar velocity observations. We show that mass selection bias from a kinetic Sunyaev–Zel’dovich velocity catalog forecasts *rms* peculiar velocities with a much more complicated  $\Omega_m$  dependency than suggested by linear perturbation theory. In addition, we show that both two-point functions for velocities disagree with linear theory predictions out to  $\sim 40 h^{-1}$  Mpc separations. A pedagogical appendix is included developing linear theory notation with respect to the two-point peculiar velocities functions.

**Key words:** cosmology: theory – cosmology: observation – cosmology: large-scale structure of the Universe – galaxies: clusters: general

## 1 INTRODUCTION

The growth of galaxy and galaxy cluster peculiar velocities provides information on the growth of structure in the gravitational instability paradigm. Over the last decade, cosmic velocity fields were an active area of research, both in observation and in theory (e.g., Bahcall & Oh (1996); Strauss & Willick (1995)). Bulk peculiar velocities of galaxies and clusters were modelled as tracers of the background dark matter velocity field and were frequently used to constrain cosmological parameters even fairly recently (?Bridle et al., 2001; Feldman et al., 2003; Juszkiewicz et al., 1999; Sheth & Diaferio, 2001; Peel & Knox, 2002).

As measured by the number of relevant papers and conferences, there has been a slightly falling interest in velocity work, in part due to observational limitations. The fundamental plane method of measuring galaxy peculiar velocities, based on methods such as Tully-Fisher and  $D_n-\sigma$ , is limited by relative intrinsic errors, which grow as a percentage of distance (Jacoby et al., 1992). For a highly selected subsample, the errors can be as low as  $\sim 10$  per cent, but in general the error is closer to 15–20 per cent of the distance. This has limited the direct use of velocities for cosmology to redshifts of  $z \simeq 0.024$ , roughly a comoving distance of  $70 h^{-1}$  Mpc (e.g., Bridle et al. (2001)) (throughout this pa-

per,  $h$  is the dimensionless hubble parameter such that today,  $H_0 = h 100 \text{ km s}^{-1} \text{ Mpc}^{-1}$ ).

In contrast, peculiar velocities derived from doppler-shifted ('kinetic') Sunyaev-Zel'dovich effect (kSZ) spectra are subject to entirely different systematic and intrinsic errors. The kSZ effect probes the hot gas within the cluster and represents a noisy estimate of the cluster's bulk motion (Holder, 2004). Complex motions of the hot gas (cold fronts, cooling flows, etc.) further increase the noise (Nagai et al., 2003). In addition, measuring the kSZ signal, which only reflects the motion of the innermost part of intracluster gas, is a challenging observational effort (Knox et al., 2004; ?); some recent experiments have achieved limited success (?). Nevertheless, as the kSZ effect is not redshift limited in principle (errors may grow *indirectly* with the distance as a function of cluster-parent halo evolution), it is a very promising technique for constraining parameters.

With the view that kSZ observational difficulties can be mitigated by sheer numbers and clever signal separation techniques, the question remains as to whether we are applying the right theoretical velocity models. Typically, linearized first order perturbation theory ("linear theory" in this paper) has been used for large scale velocity fields, although modes at the galaxy scale ( $\sim$  Mpc) are non-linear and even inter-galaxy scales ( $\sim$ 10 Mpc) are quasilinear for  $z \sim 0$ . This has been justified by only relying on the theory at larger scales where it is reasonable to invoke the stable clustering regime.

Yet clusters are assumed to exhibit large fluctuations

\* E-mail: a.peel@damtp.cam.ac.uk

at large scales and are clearly biased samples in the linear regime. How does this affect the model? In other words, what does selection bias do to the statistics of these velocities? In light of the growing body of work on non-linear halo evolution in simulations using the ‘halo model’ (Mo & White, 1996; Sheth & Tormen, 1999), peculiar velocities are due for a similar detailed examination. This is especially true for so-called ‘precision cosmology’ efforts when constraining parameters such as  $\Omega_m$  and  $\sigma_8$ . This might seem obvious in dealing with galaxy peculiar velocities. But it is also true for the streaming motions of galaxy clusters, whose rarity implies that environment dependence, biasing, and selection effects may be more important than for galaxies.

For instance, simulated clusters (large mass dark matter halos) show *rms* peculiar velocities that depart from linear theory (Colberg et al., 2000). An earlier paper found that linear theory predictions were ‘somewhat lower’ than N-body results and noted the disagreement between simulated and linear theory two-point functions (Croft & Efstathiou, 1995). Reasonable attempts to explain the excess *rms* of peculiar velocities using simulations have been published (Sheth & Diaferio (2001); Hamana et al. (2003)), although not specifically as functions of cosmological parameters. In this paper, we examine the full two-point velocity functions through N-body simulations while varying  $\Omega_m$ . Understanding the behaviour of these functions will be necessary for observations to yield constraints on parameters.

In §2, we provide a brief pedagogical discussion of linear theory peculiar velocities and discuss why linear theory is overly simplistic. We address the peak-background split approach and examine how selecting over the peaks in the density field affects theoretical predictions. In §3 we discuss our simulations. In §4 we summarize our results. We discuss our results in §5. Our conclusions in §6 also include a discussion of the usefulness of our approach for parameter forecasting in general. An Appendix is included in this paper which outlines how to calculate the two-point correlation functions for velocities of peaks.

## 2 LINEAR THEORY

### 2.1 The two-point correlation tensor

We derive the two-point velocity functions in real space (e.g., Gorski (1988)). (For mathematical elaboration, see also the Appendix in this paper.) This is crucial to properly construct the velocity correlation matrix used in any constraint analyses, as cross-correlations between velocities must be taken into account.

By ‘linear theory’, we mean that we begin with an initially Gaussian distributed field and evolve it in the linear regime of the gravitational instability paradigm via perturbation theory within a standard Friedman-Walker-Robertson universe.

With that simplification, the continuity equation

$$\mathbf{k} \cdot \mathbf{v}_k = i\dot{\delta}_k \quad (1)$$

implies that the curl-free  $v_k$  will grow as the time derivative of the density field, where  $\delta_k$  is the comoving mode of the density contrast  $\delta\rho/\rho$  and  $v_k$  is the Fourier velocity component parallel to that mode. The overdot is the conformal time derivative.

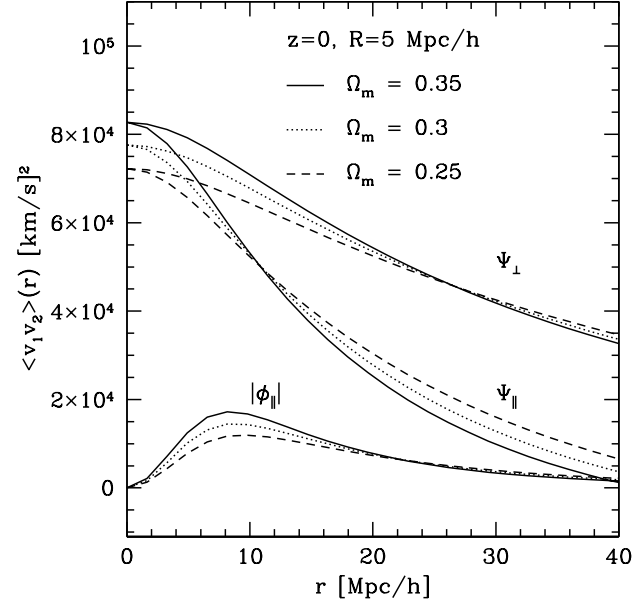


**Figure 1.** Linear theory velocity correlations of a Gaussian distributed field smoothed with a  $5 h^{-1}$  Mpc window function – all other parameters are held fixed for a flat  $\Lambda$ CDM universe. From top to bottom:  $\Psi_{\perp}$ ,  $\Psi_{\parallel}$ ,  $|\phi_{\parallel}|$  ( $\phi_{\parallel}$  is discussed in §2.3); solid, dotted and dashed lines show  $\Omega_m = 0.35$ , 0.3 and 0.25 respectively.

The two-point statistic encompasses correlations between two vectors, so we have the nine-element tensor:

$$\Psi_{ij}(r) = \langle v_i(\mathbf{x})v_j(\mathbf{x} + \mathbf{r}) \rangle \quad (i, j = 1, 2, 3) \quad (2)$$

where we invoke isotropy and homogeneity so that  $\Psi$  can only depend on the comoving distance  $r = |\mathbf{r}|$  between pairs of velocities at *comoving* positions  $\mathbf{x} = \mathbf{r}_1$  and  $\mathbf{x} + \mathbf{r} = \mathbf{r}_2$ . The  $\langle \rangle$  brackets refer to an ensemble average. It is straightforward to derive the two-point radial velocity function. On average, there are only two nontrivial correlations: one for the components of the velocities parallel to the line between them ( $\Psi_{\parallel}$ ), and one for the components perpendicular to that line ( $\Psi_{\perp}$ ). We obtain:

$$\Psi(r) = \Psi_{\perp} \hat{\mathbf{I}} + (\Psi_{\parallel} - \Psi_{\perp}) \hat{\mathbf{r}} \hat{\mathbf{r}} \quad (3)$$

where  $\hat{\mathbf{I}}$  is the identity tensor and  $\hat{\mathbf{r}}$  is the unit vector along  $\mathbf{r}$ .

Fig. 1 shows how  $\Psi_{\parallel}$  and  $\Psi_{\perp}$  depend on comoving distance between two points for three different flat  $\Lambda$ CDM cosmologies (parameters other than  $\Omega_m$  fixed;  $\Phi_{\parallel}$  is discussed below in §2.3). Note the dependence on  $\Omega_m$  is fairly degenerate with normalization such as by  $\sigma_8$ . In addition, these functions have been convolved with smoothing tophat window function to account for the velocity of an extended section of the field, rather than for a point particle.

For a given pair of *radially projected* velocities separated by angle  $\theta$  on the sky,  $v_r(\hat{\gamma}_1, r_1)$ ,  $v_r(\hat{\gamma}_2, r_2)$ , the two-point correlation is:

$$\begin{aligned} \Psi_{12} &\equiv \langle v_{r1} v_{r2} \rangle = \hat{\gamma}_1 \cdot \Psi \cdot \hat{\gamma}_2 \\ &= \Psi_{\perp} \cos \theta + (\Psi_{\parallel} - \Psi_{\perp}) f(\theta, r_1, r_2) \end{aligned} \quad (4)$$

where:

$$\cos \theta = \hat{\gamma}_1 \cdot \hat{\gamma}_2 \quad (5)$$

and

$$f(\theta, r_1, r_2) = \frac{(r_1^2 + r_2^2) \cos \theta - r_1 r_2 (1 + \cos^2 \theta)}{r_1^2 + r_2^2 - 2r_1 r_2 \cos \theta}. \quad (6)$$

For the extreme cases of either two positions lined up along the line of sight:

$$\theta \rightarrow 0 \text{ and } r_1 \neq r_2 \quad f \rightarrow 1 \\ \Psi_{12} = \Psi_{\parallel} \quad (7)$$

or for two positions at the same radial distance, but separated by a small angle:

$$\theta \neq 0 \text{ but small and } r_1 = r_2 \quad f \rightarrow -\frac{\theta^2}{4} \\ \Psi_{12} = \left(1 - \frac{\theta^2}{4}\right) \Psi_{\perp} - \frac{\theta^2}{4} \Psi_{\parallel} \approx \Psi_{\perp}. \quad (8)$$

The zero-lag for either two-point function is related to the *rms* velocity:

$$\sigma_v^2 = \langle v^2 \rangle = \langle \mathbf{v}(\mathbf{x}) \cdot \mathbf{v}(\mathbf{x}) \rangle = \Sigma_i \langle v_i^2 \rangle = 3\Psi_{(\parallel \text{ or } \perp)}(0) \quad (9)$$

where we note that the literature often uses  $\sigma_v^2$  and  $\langle v^2 \rangle$  interchangeably.

## 2.2 Arguments against linear theory

The naïve idea that linear theory in the field will predict the velocities of galaxies should be suspect, though this has been the norm in the past (with some notable exceptions, e.g., Ma & Fry (2002), ?). Galaxies are not only non-linear objects themselves, their velocities are often responding strongly in the non-linear regime since perhaps as many as  $\sim 20$  per cent of them are in bound groups. Furthermore, they most likely represent biased objects compared to the general behaviour of the dark matter background. Data from large scale surveys has been consistent with modelling this bias as approximately linear for  $L_*$  (and dimmer) galaxies (Seljak & Warren, 2004), though simulations suggest the bias is expected to increase for larger sized haloes (Seljak et al., 2004).

Clusters are on average inherently rare objects as modelled by any Press-Schechter type formalism. Although a  $10^{14} h^{-1} M_{\odot}$  cluster began in a comoving volume of radius  $R \simeq 7 h^{-1} \text{ Mpc}$  ( $\Lambda$ CDM), few such volumes have clusters. In fact, a cluster is found at late times (on average) in a radius  $\sim 4$  times that size, i.e., a volume 64 times the original source volume for the cluster. This implies that galaxy clusters as a selected sample should have a bulk motion which is responding to long wavelength modes which have not undergone collapse and are therefore well-modelled in the linear approximation.

The statistical rarity of high mass haloes is presumed to be a source of a suppression factor to their *rms* velocity as predicted by the excursion hierarchy approach of Bardeen et al. (1986). Modeling clusters as originating from the 3- $\sigma$  (or greater) end of the density peak distribution, the peak *rms* velocity is given in linear theory by:

$$\sigma_p^2(R) = \left(1 - \frac{\sigma_0^4(R)}{\sigma_1^2(R)\sigma_{-1}^2(R)}\right) \sigma_v^2(R) \quad (10)$$

where:

$$\begin{aligned} \sigma_n^2(R, \eta) &= \int \frac{k^2 dk}{2\pi^2} P(k, t) k^{2n} W^2(kR) \\ &= D^2(\eta) \int \frac{k^2 dk}{2\pi^2} |\delta_{k,0}|^2 k^{2n} W^2(kR). \end{aligned} \quad (11)$$

Implicit in the final form above is the linear theory assumption that  $\delta(\mathbf{x}, \eta)$  is separable; thus  $\delta(\mathbf{x}, \eta) = D(\eta)\delta_0(\mathbf{x})$  and we choose the growth function  $D$  to be normalized to one today. ( $D = a$  for an  $\Omega_m = 1$  cosmology). This assumption is reasonable if we smooth on large enough scales to ignore nonlinear processing on small scales, which is the purpose of the window function  $W(kR)$ . The window function is usually chosen to be the Fourier transform of either a Gaussian or tophat envelope. When the time ( $t$  or  $\eta$ ) is not specified,  $D$ , or  $P(k)$  assume values at redshift zero, i.e., today. For examples of this notation, the cosmological parameter  $\sigma_8 = \sigma_0(8 h^{-1} \text{ Mpc})$ , and the  $\sigma_v$  of Eqs. (9) and (10) above is  $\propto \sigma_{-1}$ .

The *rms* velocity of rare, massive objects is apparently suppressed by a few to ten percent compared to background as implied by Eq. (10). Colberg et al. (2000) show that although this statement agrees for the velocities of the density peaks at early times, large mass haloes evolved to low redshift which formed around these peaks actually have a higher *rms* velocity than linear theory would have predicted by as much as 40 per cent. This discrepancy is observed in our simulations even at moderate redshifts ( $z \gtrsim 0.6$ ) in cluster formation and will be discussed in §5 below. See the Appendix for more detailed calculations to predict peak-peak velocity correlations as a natural extension to Eq. (10); however, it is fairly clear from simulations that the peak-background split approach is not accurate at late times, as evidenced for example with the *rms* peak velocity above.

How does one take into account the bias for dense objects, like galaxies and clusters, caused by their being in an overdense region? In general, an object's peculiar velocity is greatly affected by its environment: haloes in overdense regions typically move faster than those in less dense ones (Colberg et al., 2000; Sheth & Diaferio, 2001; Hamana et al., 2003). Although the average intracluster distance is large, the likelihood of finding a cluster near another is high, and of finding a cluster near a large overdensity of galaxies and groups is very high. If environment plays an important role for the evolution of galaxy peculiar velocities, it must therefore play an even more important one for clusters.

## 2.3 Momentum correlations

A heuristic way to see the effect of this selection bias is to re-examine Eq. (1) within the context of linear theory. The full form, after separating out the background solution and regardless of the amplitude of  $\delta(x)$  is:

$$\dot{\delta} + \nabla \cdot [(1 + \delta)\mathbf{v}] = 0. \quad (12)$$

This suggests we might consider the statistic:

$$\begin{aligned} \tilde{\Psi} &= \langle \tilde{\mathbf{v}}(\mathbf{x}) \tilde{\mathbf{v}}(\mathbf{x} + \mathbf{r}) \rangle \\ &= \langle \mathbf{v}(\mathbf{x})(1 + \delta(\mathbf{x})) \mathbf{v}(\mathbf{x} + \mathbf{r})(1 + \delta(\mathbf{x} + \mathbf{r})) \rangle \\ &= \langle \mathbf{v}_1 \mathbf{v}_2 \rangle + \langle \mathbf{v}_1 \mathbf{v}_2 \delta_1 \rangle + \langle \mathbf{v}_1 \mathbf{v}_2 \delta_2 \rangle + \langle \mathbf{v}_1 \delta_1 \mathbf{v}_2 \delta_2 \rangle \end{aligned} \quad (13)$$

where the subscripts ‘1’ and ‘2’ correspond to the arguments  $\mathbf{x}$  and  $\mathbf{x} + \mathbf{r}$  respectively. This is a ‘momentum correlation’, i.e., weighting the velocity by the density in the region.

Evaluating Eq. (13) using arguments within linear theory solely to build intuition (i.e., three-point functions are zero, ignoring the connected part of the four-point function, etc.) leads to:

$$\tilde{\Psi}(r) = \Psi_{\perp}(1 + \xi(r))\hat{\mathbf{I}} + ((\Psi_{\parallel} - \Psi_{\perp})(1 + \xi(r)) + \Phi_{\parallel})\hat{\mathbf{r}}\hat{\mathbf{r}} \quad (14)$$

with  $\Psi_{\perp}$  and  $\Psi_{\parallel}$  as before, and:

$$\begin{aligned} \Phi_{\parallel} &= \langle \mathbf{v}_1 \delta_2 \rangle \langle \mathbf{v}_2 \delta_1 \rangle \\ &= -\frac{\dot{D}_1 \dot{D}_2 D_1 D_2}{4\pi^4} \left\{ \int dk |\delta_{k,0}|^2 k j_1(kr) W^2(kR) \right\}^2 \end{aligned} \quad (15)$$

$\xi(r)$  is the usual Fourier transform of the power spectrum:

$$\xi(r) = \langle \delta_1 \delta_2 \rangle = D_1 D_2 \int \frac{k^2 dk}{2\pi^2} |\delta_{k,0}|^2 j_0(kr) W^2(kR). \quad (16)$$

Fig. 1 shows the behaviour of  $|\Phi|$  at  $z=0$ .

So how does Eq. (14) compare to the unweighted model, Eq. (3)? The extra factor of  $\xi$  boosts the correlations for velocities at short ( $\sim 10 h^{-1}$  Mpc) separations. The new factor of  $\Phi_{\parallel}$  which is zero at both zero lag and large separations boosts the anticorrelations in  $\Psi_{\parallel}$  for a characteristic separation. This is not presumed to be exact, but will aid discussion of results in §5.

By definition, linear theory becomes invalid when  $\delta \sim 1$  which forces the equations in Fourier space to mix modes. This is where numerical simulations become essential.

#### 2.4 Previous efforts regarding the velocity *rms*

Extensive work by Sheth & Diaferio (2001) and Hamana et al. (2003) comparing halo velocities in simulations to linear theory showed that the local environment of a halo had a heavy influence on the evolution of its velocity. Specifically, the bias predicted by the halo model suggested that halo velocities would likely be boosted as if they had evolved in a higher- $\Omega_m$  universe (see Fig. 1) because haloes are typically found in overdense regions.

In one approach (Sheth & Diaferio, 2001), it was suggested that a typical halo speed today would be related to the linear growth velocity (evolved from redshift 20 until today) boosted by the local density in the region:

$$v_0 = (1 + \delta)^{\mu(R)} \frac{\dot{D}(\eta_{20})}{\dot{D}(\eta_0)} v_{20} \quad (17)$$

where  $\delta$  is smoothed over a region of radius  $R$  using a Gaussian window function. They found that  $\mu$  was naturally tied to the choice in smoothing radius, and for their simulations, fit:

$$\mu(R) = 0.6 \frac{\sigma^2(R)}{\sigma^2(10 h^{-1} \text{ Mpc})}. \quad (18)$$

Following this guideline, the second approach (Hamana et al., 2003) found a similar result phrased as the *rms* velocity (essentially the same statistic: see the final paragraph in §2.1 above):

$$\sigma_{halo}^2(M, \delta) = [1 + \delta(R_{local})]^{2\mu(R_{local})} \sigma_v^2(M) \quad (19)$$

although neither group found the velocities to have a strong dependence on halo mass.

In the first work, the choice of  $10 h^{-1}$  Mpc as a reference scale for smoothing is motivated by the fact that it roughly represents the transition from linear to non-linear regimes today as measured by  $\sigma(R) \sim 1$ . According to the second work, deciding how to choose  $R_{local}$  is primarily an *ansatz*.

The velocity statistics in previous papers investigated a wider range of dark matter halo masses. We will focus on the statistics of only the largest mass haloes by imposing a mass cutoff suggested from models of the Sunyaev–Zel’dovich effect (Carlstrom et al., 2002). In addition, we will examine this selection effect on the full two-point functions, rather than simply the zero-lag.

### 3 SIMULATIONS

#### 3.1 ART code

We used an Adaptive Refinement Tree (ART) N-body code (Kravtsov, 1999) which, like its predecessor Particle Mesh (PM) N-body codes, integrates trajectories of collisionless particles by solving the Poisson equation. Unlike PM codes, ART allows for a hierarchy of refinement meshes where collapsed objects require more resolution.

ART employs standard particle-mesh techniques to compute acceleration grids in order to advance particle coordinates and velocities in time. A regular cubic grid covers the entire computational volume and defines the initial minimum resolution of the simulation. This grid is then refined where the density contrast is higher to form higher resolution sub-meshes in those regions of interest. The main computational loop of the integration consists of: (1) density assignment for all existing meshes; (2) running the gravitational solver; (3) routine updating particle positions and velocities; (4) modifications to the mesh hierarchy.

#### 3.2 Halo finder algorithms

The ART codes we used produce files of particle positions and velocities which were subsequently analysed for the presence of haloes. The basic problem of halo finding in a simulation is that there are no clear boundaries for haloes. There is no single perfect algorithmic definition of a group or mass of a group.

Many halo finding algorithms exist, but tend to fall into two categories: the friends of friends type (FoF) linked-list type approaches where particles are identified with a halo if they are within a certain chosen distance of each other (Efstathiou et al., 1985); and overdensity methods such as DENMAX which calculates the density as a function of a grid and identifies to which local maximum each particle belongs (Bertschinger & Gelb, 1991). We used a relatively recent method named HOP (Eisenstein & Hut, 1998) which follows the logic behind overdensity methods yet includes ‘hopping’ to nearest neighbors *à la* FoF methods. Instead of calculating the density on a grid, a density is associated with each particle. Then a search is conducted for the highest density nearest neighbor until a particle is its own densest neighbor. All particles which trace to the same such particle are grouped. A followup ‘regrouping’ then reunites any

sufficiently bound haloes which happen to contain two (or more) local maxima such that the initial hopping misidentified them as separate haloes.

### 3.3 Virial radius

After HOP was used to find the haloes, a crude spherical overdensity method was applied to restrict the statistics to different cutoff radii. Real measurements of cluster peculiar velocities via the *kSZ* effect will be restricted to the baryons at the core but are likely to represent at best the bulk motion of particles ‘trapped’ within the virial radius (Holder et al., 2001). We define the virial radius by beginning nearest the central overdensity of a halo and including particles at every increasing radii until the overdensity within that radius is 180 times the background density.

### 3.4 Preliminaries

The first questions to answer using N-body simulations were to determine: (1) how many high-mass haloes (presumably hosting clusters) were needed; (2) how big the simulated volume should be; and (3) how much mass resolution was required for each halo. This phase was completed using approximately 10,000 hours of processor time on the the IBM SP computer, ‘Seaborg’, at the National Energy Resource Computing Facility at Lawrence Berkeley National Laboratory.

#### 3.4.1 Number of high mass haloes (clusters)

We relied on linear theory predictions as a rough guide in determining the number of high mass ( $M \gtrsim 3 \times 10^{14} M_{\odot}$ ) haloes we would need to achieve an error variance on the order of a percent for  $\Omega_m$ .

For effectively uncorrelated cluster velocities, from, e.g., a very sparse survey, we estimate the expected error variance on  $\Omega_m$ . From a measurement of  $N$  clusters with their peculiar velocity variance represented by the zero-lag value of either two-point function ( $\Psi_0(z_i)$ ):

$$\begin{aligned} (\Delta\Omega_m)^2 &= \left( \sum_i \left( \frac{\partial\Psi_0(z_i)}{\partial\Omega_m} \right)^2 \frac{1}{2(\Psi_0(z_i) + \sigma_{v,noise}^2)^2} \right)^{-1} \\ &\simeq \frac{800}{N} (.01)^2 \end{aligned} \quad (20)$$

where the last equality assumes  $N$  clusters with  $\sigma_{v,noise}^2 \ll \Psi_0$  all at  $z=1$ , and  $\partial\ln\Psi_0/\partial\Omega_m \simeq 5$  (Peel & Knox, 2002). Thus, on the order of 1000 clusters would be apparently sufficient to constrain  $\Omega_m$  to a few percent. Current and future cluster surveys expect to detect on the order of 10,000 clusters through the Sunyaev-Zel’dovich effect (Carlstrom et al., 2002).

#### 3.4.2 Volume

To determine the necessary volume to find these haloes, we followed Jenkins (Jenkins et al., 2001) fitting formula for the ‘universal mass function’:

$$f(M) = 0.315 \exp(-|\ln\sigma^{-1} + 0.61|^{3.8}) \quad (21)$$

where  $\sigma^2(R)$  is the usual smoothing of the power spectrum with a window function  $W(kR)$ , and the number of haloes of mass  $M$  at a redshift  $z$  is:

$$\frac{dn}{dM}(M, z) dM = 2 \frac{\bar{\rho}}{M} \nu f(\nu(M)) d\nu \quad (22)$$

where

$$\nu = \delta_c / \sigma(M) \quad (23)$$

and  $\delta_c$  is the critical value of a spherical overdensity at turnaround time. The universality referred to is due to the functional form of  $f$  and is not as useful for our purposes as Eq. (22) above. For 300 high mass clusters ( $3 \times 10^{14} h^{-1} M_{\odot}$ ) at a redshift of  $z \sim 0.6$ , we required a fairly large volume of  $(850 h^{-1} \text{ Mpc})^3$ . The steepness of the halo mass function would then guarantee  $\sim 10^3$  clusters with mass greater than  $2 \times 10^{14} h^{-1} M_{\odot}$  at  $z \sim 0.6$ .

#### 3.4.3 Number of particles per halo

We simulated a volume with the same initial conditions but with three different mass resolutions to see how many particles were needed to resolve halo velocities. For this convergence test, we used smaller boxes of  $150 h^{-1} \text{ Mpc}$  per side for speed. At this size, we expected very few haloes above  $10^{14} h^{-1} M_{\odot}$  at a redshift of  $z \sim 0.6$ .

Beginning with  $256^3$  cells, we used number of particles  $64^3$ ,  $128^3$  and  $256^3$  and tracked the velocities of the top five haloes as they became more resolved, as well as the *rms* of the entire population of haloes. From this convergence test, it became clear that the number of dark matter particles required to resolve a velocity was approximately 70, which meant that for an  $850 h^{-1} \text{ Mpc}$  sized box,  $(256)^3$  particles would be sufficient to resolve the velocities of the largest haloes, i.e., those haloes most likely to contain massive clusters. Eight  $425 h^{-1} \text{ Mpc}$  per side simulations would cover the same volume and run much faster, but with the loss of the  $k = 2\pi/850 h \text{ Mpc}^{-1}$  mode. We ran multiple  $425 h^{-1} \text{ Mpc}$  per side simulations with  $128^3$  particles and compared results with one  $850 h^{-1} \text{ Mpc}$  using  $256^3$  particles. We found that losing the low- $k$  mode ( $k = 2\pi/850 h \text{ Mpc}^{-1}$ ) had a negligible effect on velocity statistics.

For our chosen resolution of  $128^3$  particles realized in ten  $(425 h^{-1} \text{ Mpc})^3$  volume boxes,  $m_p = 3.0 \times 10^{12} h^{-1} M_{\odot}$  ( $\Lambda\text{CDM}$ ,  $\Omega_m=0.3$ ). This means that any halo identified with approximately 60 particles ( $1.8 \times 10^{14} h^{-1} M_{\odot}$ ) is a halo capable of hosting a cluster. The simulations were run using three values of  $\Omega_m$  (0.25, 0.3, 0.35) in flat  $\Lambda\text{CDM}$  cosmologies with all other parameters fixed on the UK National Cosmology Supercomputer in Cambridge. Each realization took less than one week on eight Altix 3700 Itanium2 processors. (Eight Altix processors was approximately ideal for this number of particles and timesteps.) We discuss the broad usefulness of this approach in §6.

## 4 RESULTS

Table 1 summarizes the the *rms* peculiar velocity and number of haloes found above the cutoff mass as a function of cosmology in our total volume ( $10 \times (425)^3 \simeq (915 h^{-1} \text{ Mpc})^3$ ). For brevity, we will initially display

**Table 1.** Number and Peculiar Velocities of High Mass Haloes from N-body Simulations

z	N(> $10^{14.26} h^{-1} M_{\odot}$ )			$\sigma_v$ [km s $^{-1}$ ]		
	$\Omega_m$			$\Omega_m$		
	0.25	0.3	0.35	0.25	0.3	0.35
0.0	9344	12618	16541	532	539	534
0.25	6211	8235	10530	554	552	543
0.667	2320	3009	3790	555	542	536
1.5	109	131	146	563	522	462

our results in the context of only one cosmology, a flat  $\Lambda$ CDM with  $\Omega_m=0.3$ . We first consider the Gaussianity of the one-dimensional velocity distribution (and the related Maxwellian speed distribution) to justify error estimates. Then we show the zero lag portion of the two-point functions: the *rms* peculiar velocities as a function of mass and density. Following this, we reveal the primary result of this work: the redshift evolution of the two-point functions for haloes above a cutoff mass. At that point, we will also introduce our results from two other cosmologies, flat  $\Lambda$ CDM with  $\Omega_m=0.25$  and 0.35. We conclude this section by showing the bulk velocity history of the particles which make up the zero redshift haloes above a cutoff mass. We discuss and explain the results in §5.

Only haloes with a minimum mass of  $1.8 \times 10^{14} h^{-1} M_{\odot}$  (60 particles in our fiducial  $\Omega_m=0.3$  runs) were used to ensure reliable velocities (see §3.4.3 above). Our conclusions will not depend on this low mass estimate for a cluster capable of producing a measurable Sunyaev–Zel’dovich effect; in fact, they would be more dramatic for higher mass cutoffs. After identifying haloes by their member particles as described above, we calculated the bulk flow peculiar velocity by averaging particle velocities within the virial radius, defined as the spherical radius for which the halo is 180 times the background density. The resulting velocity vector is then used to calculate all halo velocity statistics.

To understand how appropriate linear theory is for certain scales (and as a consistency check on our simulations), we also track the average velocities and two-point functions for the field. To do this, each simulation is partitioned into equal-sized boxes and the particle velocities within each box are averaged to create a ‘bulk’ peculiar velocity. The process is repeated for different smoothing lengths. We coin these partitions ‘miniboxes.’ The statistics of these minibox bulk velocities represented a simulated version of linear theory, convolved with cubic window functions.

This partitioning was repeated for different nominal linear sizes of  $L = 8\text{--}128 h^{-1}$  Mpc by powers of two. Since the simulations were of linear size  $425 h^{-1}$  Mpc, these lengths were rescaled due to roundoff to 8.02, 16.3, 32.7, 70.8, and  $142 h^{-1}$  Mpc so that the entire volume would be sampled. These values correspond to tophat-sphere smoothing volumes with radii of 4.98, 10.1, 20.3, 43.9 and  $87.9 h^{-1}$  Mpc. This was tested by examining the theory calculation with either a boxcar window function or a tophat window function. In either case the same theoretical results were obtained when the volumes of the respective cubes or spheres in real space were equivalent. Each minibox was then assigned a density based on the number of particles found inside:  $\delta_i = n_i/\bar{n} - 1$ . Attempts to look at miniboxes of

smaller extent were limited by the spatial resolution of the simulation.

Three things should be mentioned about how the linear theory was calculated. First, the apparent dependence on mass shown in the downward curvature of the linear theory is due to convolving the integral in Fourier space with a tophat window function  $W(kR)$ , with a mass associated with the comoving volume  $4\pi R^3 \bar{\rho}/3 = M$  in contrast to the smaller smoothing radii used by Croft & Efstathiou (1995). Secondly, the suppression factor mentioned in §2.2 above is completely ignored as we are comparing linear theory only to the entire particle field through the minibox statistics. Finally, the integration limits in Fourier space were chosen to match the simulation: the lowest frequency associated with the size of the box represents the lower bound on the  $k$ -integrals and the upper limit value was chosen to reflect the Nyquist frequency. Initially, the Nyquist frequency was simply  $2\pi/425 \times 128/2 h \text{ Mpc}^{-1} \approx 1 h \text{ Mpc}^{-1}$ . While the dynamic mesh was resolved by as many as six times at late redshifts, those new distances represent collapsed regions and do not force much of an increase in the Nyquist frequency for integrating the linear power spectrum. Since we integrate with a window function, the effect of using  $1 h \text{ Mpc}^{-1}$  *vs.*  $(2^6) = 64 h \text{ Mpc}^{-1}$  for the upper limit is negligible.

#### 4.1 Gaussianity of velocity distributions

We examine velocity distributions at redshifts  $z = 0$  for haloes and miniboxes in order to understand relevant confidence intervals for  $v^2$ . If the set of one dimensional velocities  $\{\mathbf{v}_i \cdot \hat{x}, \mathbf{v}_i \cdot \hat{y}, \mathbf{v}_i \cdot \hat{z}\}$ , is Gaussian, then  $\{v_i^2\}$  should fit a Maxwellian distribution. Figs. 2 and 3 below show that Gaussian (and related Maxwellian) distributions work reasonably well for both field (as represented by miniboxes) and halo one-dimensional velocities (and related 3-d speeds), even for different mass ranges. The bias seen in Sheth & Diaferio (2001) between smaller and larger haloes is much less apparent for masses above  $\sim 10^{14} h^{-1} M_{\odot}$ . Both distributions are fit by a Maxwellian with one-dimensional velocity dispersion of  $311 \text{ km s}^{-1}$ , i.e., an *rms* of  $\sqrt{\langle v^2 \rangle} = \sqrt{3}\sigma_{v1} = 539 \text{ km s}^{-1}$ . The shot noise from rarity at higher redshift for a large Sunyaev–Zel’dovich survey clearly implies a transition to a Poisson distribution when the data is binned in redshift. This is also true from our work, but is not shown here for brevity.

There is a high velocity tail, as predicted by Sheth & Diaferio (2001). However, for our large number of cluster-sized haloes, the majority of the distribution is still well enough fitted to a Maxwellian to justify the  $1-\sigma$  errors in the figure below given by:

$$\langle v^4 \rangle = \left[ \frac{2}{N} \right] \langle v^2 \rangle^2. \quad (24)$$

In the case of the two-point function, this becomes:

$$\langle \Psi_{\perp,\parallel}^2(r) \rangle = \frac{2}{N} |\Psi_{\perp,\parallel}(r) \Psi_{\perp,\parallel}(0)|. \quad (25)$$

#### 4.2 Velocity rms

Fig. 4 shows the *rms* velocities of miniboxes and haloes *vs.* linear theory predictions as functions of mass at differ-

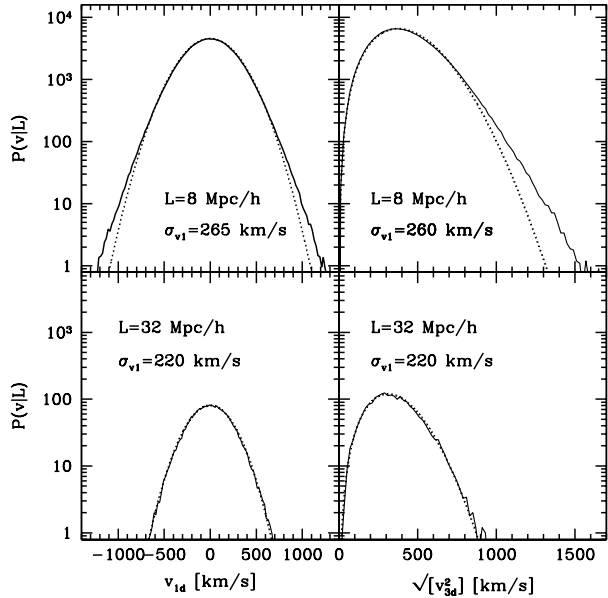


**Figure 2.** One-dimensional velocity distributions (left) ( $[v_x, v_y, v_z]$ ) and speed distribution (right) for miniboxes smoothed over  $8.02 h^{-1}$  Mpc (top) and  $32.7 h^{-1}$  Mpc at redshift 0. Matching Gaussian and Maxwellian distributions for the one-dimensional velocities and speed respectively are shown as dotted lines. Recall that  $v_{rms} = \sqrt{3}\sigma_{v1}$ .

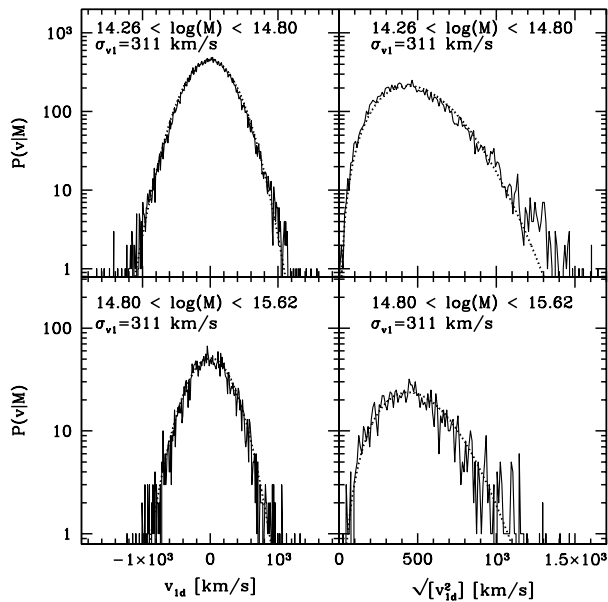


**Figure 3.** As above, but for haloes binned in two mass ranges at redshift 0.

ent redshifts. In the mass range of interest ( $10^{14}$  – few  $\times 10^{15}$ ) linear theory and the minibox velocity statistics are in excellent agreement. Although not shown for brevity, the minibox two-point functions were also in agreement with linear theory.

This figure also shows the discrepancy between  $rms$  velocities of linear theory and haloes. This is in rough agree-

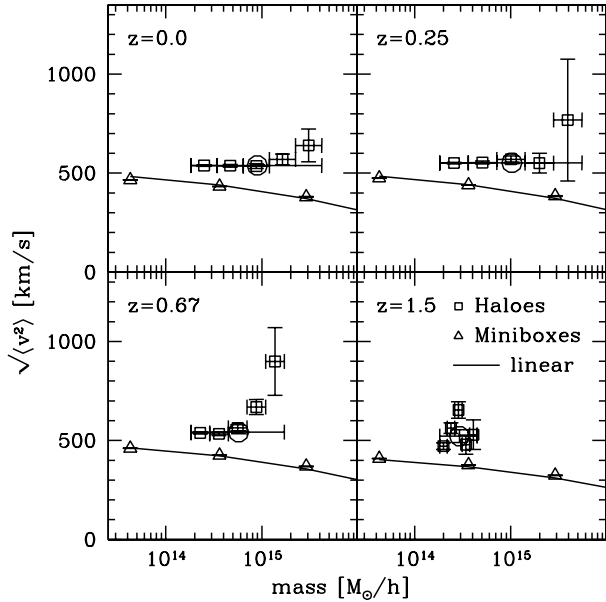


**Figure 4.** Peculiar velocity  $rms$  as a function of mass: boxes show halo statistics; triangles show minibox statistics; solid lines show linear theory. The circle shows the average halo statistic for the entire mass range of interest with insignificant statistical 1-sigma error bar.

ment with the result that linear theory underpredicts the  $rms$  of cluster peculiar velocities as represented by massive dark matter haloes by a large percent. For example, averaged across the mass range, the predicted value of halo  $rms$  peculiar velocity is  $539 \pm 3$   $km\ s^{-1}$  at redshift zero, whereas linear theory predicts an average of  $415$   $km\ s^{-1}$  in that range, a discrepancy of 30 per cent. In agreement with Sheth & Diaferio (2001) and Hamana et al. (2003), we find essentially no mass dependence for the  $rms$  peculiar velocities (within  $1-\sigma$ ). Since linear theory *does* predict a weak dependence on mass (larger objects should be *slower* as shown by the convex line in Fig. 4) the discrepancy found by Colberg et al. (2000) actually worsens for the largest mass haloes, although clearly this is of less statistical significance.

#### 4.3 Two-point functions

We show the two-point function redshift dependence in two ways. First, motivated by observations, we examine the haloes above a cutoff mass which have collapsed at redshifts  $z=0.0$ ,  $0.25$  and  $0.667$ , shown in Figs. 5, 6, 7, respectively. We also examine the velocity *history* of the particles which will be within the virial radius of  $z=0$  haloes above the mass cutoff. We do this by calculating particles' 'bulk' velocity as if they had formed haloes already. We only use those particles which will be within the virial radius at  $z=0$ . Those results at redshifts  $z=0.25$ ,  $0.667$  and  $19$  are shown in Figs. 8, 9, 10, respectively.

For Figs. 5 through 9, we use linear theory smoothed over  $R = 10 h^{-1}$  Mpc as a benchmark for comparison, though we do not *a priori* expect halo velocity statistics to be in agreement with linear theory. This raises the question as to what the appropriate comparison smoothing scale

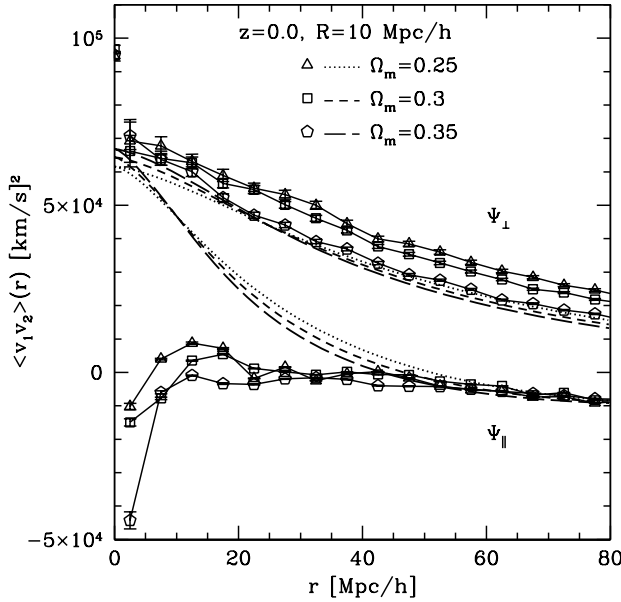


**Figure 5.** Halo velocity two-point correlations (perpendicular and parallel components) at redshift  $z = 0.0$  for haloes above the mass cutoff (see text). The dotted, short-dashed and long-dashed lines show linear theory and the triangles, squares and pentagons show simulated haloes for  $\Omega_m = 0.25, 0.3$ , and  $0.35$  respectively. Note the high value for simulations at the zero lag (where  $\Psi_\perp$  must equal  $\Psi_\parallel$ ).

should be. The average distance at  $z=19$  of the particle farthest from the eventual halo centre was calculated to be  $11.81, 11.23$  and  $10.64 h^{-1}$  Mpc for cosmologies  $\Omega_m = 0.25, 0.3$ , and  $0.35$  respectively. Fig. 10 shows these values rather than  $R = 10 h^{-1}$  Mpc which would reflect larger values of the two-point function at zero lag (by approximately 5 per cent). (Larger values of the smoothing scale suppress the linear two-point functions more at short-distances.)

#### 4.3.1 $\Psi$ as functions of redshift and cosmology

Examining the two-point functions for different  $\Omega_m$  values at different redshifts, four crucial results stand out. First, looking at Table 1, it is essentially impossible to discriminate between these three different cosmologies at zero lag at redshift  $z=0$ , in contrast to the behaviour predicted by linear theory (Peel & Knox, 2002). Second, at higher redshifts, the *rms* peculiar velocity dependence on  $\Omega_m$  for these three values is exactly opposite to that expected from linear theory (see Fig. 1). Third, the behaviour of the parallel component shows heavy influence from infall for  $r < 30 h^{-1}$  Mpc at *any* redshift for which these massive haloes exist. In particular, the extreme anticorrelation seen in Fig. 7 at  $r \sim 4 h^{-1}$  Mpc is comparable (or larger) in magnitude to the zero lag value shown. Fourth, for the three values of  $\Omega_m$  the perpendicular components alone seem to reflect linear theory closely in behaviour if not in amplitude.

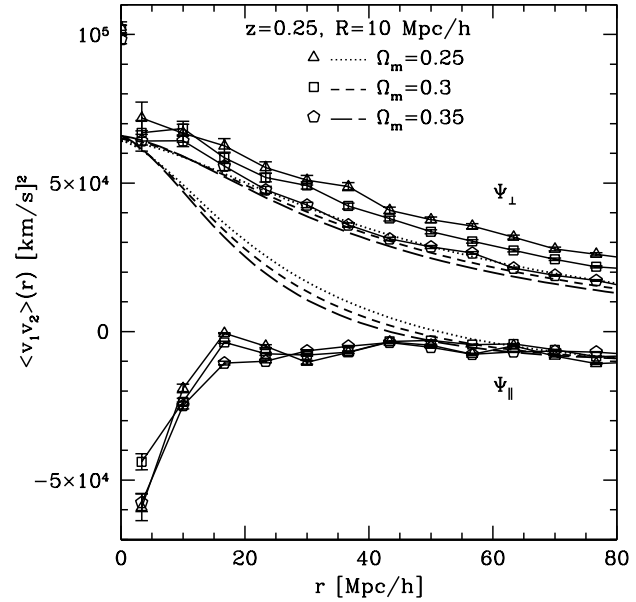


**Figure 6.** as above, but for  $z = 0.25$ .

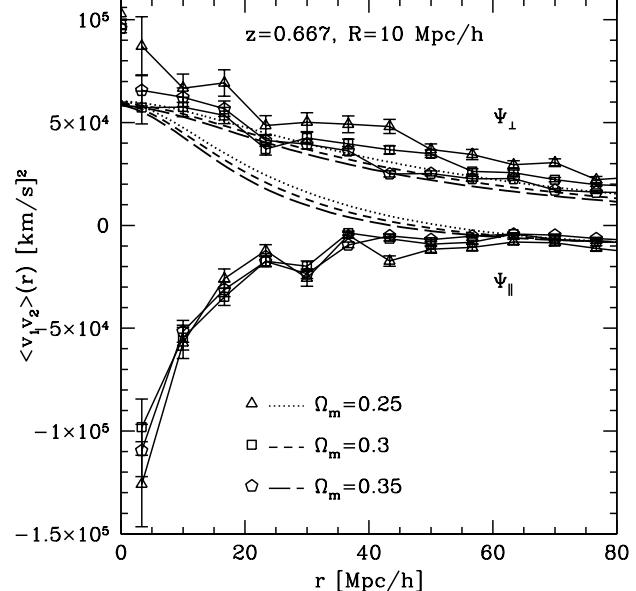


**Figure 7.** as above, but for  $z = 0.667$ .

#### 4.3.2 $\Psi$ as functions of history

Tracking the history of the particles which will assemble the largest haloes by  $z=0$  (as well as those at higher redshift), it is clear that the parallel component shown in Figs. 8 and 9 does not reflect the infall as strongly as seen in Figs. 6 and 7. Note also that the parallel component shows remarkably little difference in behaviour (apart from amplitude) between  $z=19$  and  $z=0.667$ . Prior to the assembly of the largest haloes, the gross behaviour of their particles is nearly fixed to track linear theory. Only just as and after a halo viri-

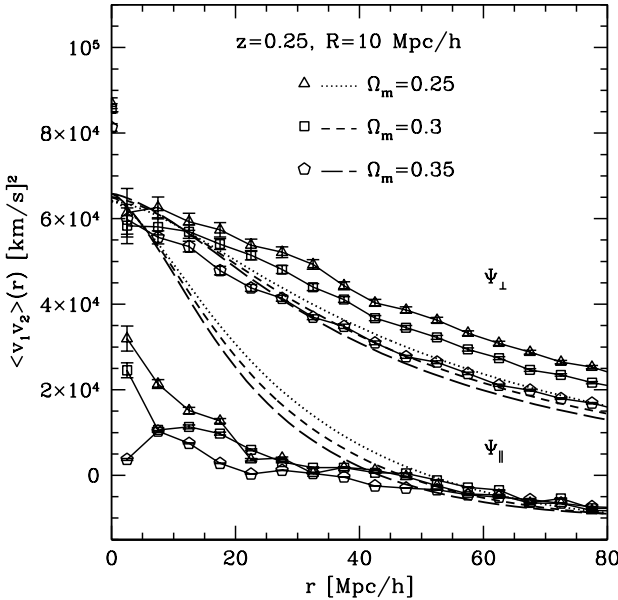


**Figure 8.** Velocity two-point correlations at  $z = 0.25$  (perpendicular and parallel components) for the groups of particles which will be in the haloes shown in the Fig. 5. The dotted, short-dashed and long-dashed lines show linear theory and the triangles, squares and pentagons show simulated haloes for  $\Omega_m = 0.25$ , 0.3, and 0.35 respectively. Note the high value for simulations at the zero lag (where  $\Psi_{\perp}$  must equal  $\Psi_{\parallel}$ ).

alizes does the strong infall out to  $r < 30 h^{-1}$  Mpc become apparent. This is discussed in §5 as a coincidence in timing.

In Fig. 10, the *rms* peculiar velocity is *smaller* than linear theory predictions (and would be even smaller if we had retained  $R = 10 h^{-1}$  Mpc smoothing). This suppression is comparable to the excursion heirarchy suppression proposed by Bardeen et al. (1986) mentioned in §2.2 above. The jump between the perpendicular component at  $r \gtrsim 2 h^{-1}$  Mpc and the *rms* value at  $r=0$  is just as abrupt as it is at later redshifts. Some of this may be explained as an artefact of resolution (recall the average interparticle separation is  $3 h^{-1}$  Mpc). Nonetheless, the perpendicular component for the particles destined for large haloes is actually less like linear theory here than at any subsequent time.

## 5 DISCUSSION

There are at least three different factors which help explain the differences between cluster-sized dark matter halo peculiar velocity two-point functions at different values of  $\Omega_m$  and their differences from the two-point functions predicted by linear theory. Specifically, there are two selection biases to consider as well as the effect of dark energy domination. The first selection bias (also considered in previous work) is that regions which harbor the seeds of large dark matter haloes are by definition overdense. This helps explain why the *rms* peculiar velocity is 30 per cent higher than predicted by linear theory at any redshift in which one would find such a virialized large dark matter halo.

The second, more subtle selection bias strongly affects

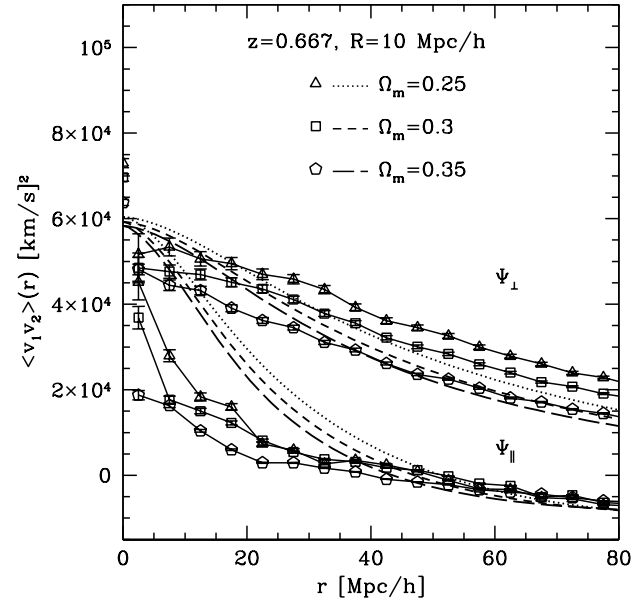


**Figure 9.** as above, but for  $z = 0.667$ .

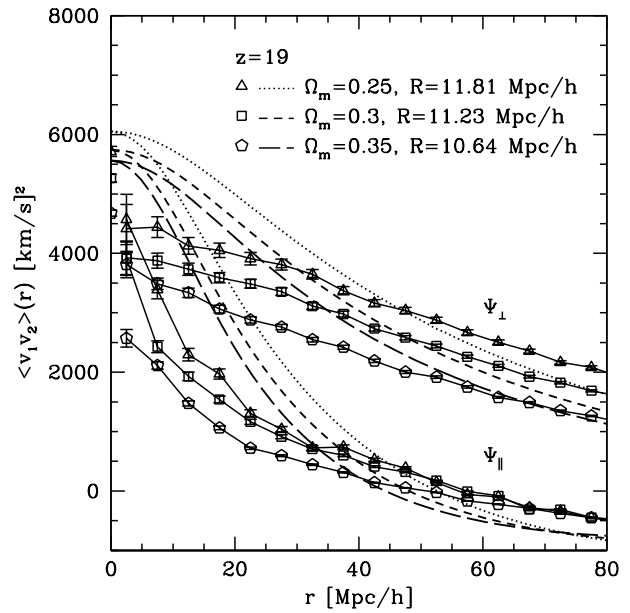


**Figure 10.** as above, but for  $z = 19$ .

the constraining power of a galaxy cluster-based set of velocity observations. The rarity of large haloes is sensitive to a combination of  $\Omega_m$  and  $\sigma_8$ . If one fixes the value of  $\sigma_8$  but decreases the value of  $\Omega_m$ , there is an effective transfer of power from small scales to large ones. This creates deeper initial potential wells at the (now rarer) largest scales and thereby increases the acceleration of halo velocities. The largest mass haloes will preferentially be found near these large rare fluctuations. If we could calculate the velocity statistics using *all* haloes down to galaxy size (many of which are not responding to the extremely rare, deep, large-scale potentials), we

would find that there was a decrease in the velocity power at small scales and would recover the expected  $\Omega_m$  dependence predicted by linear theory. However, the hot plasma necessary to produce a Sunyaev–Zel’dovich effect observation requires a deep potential well and is therefore sensitive to a specific halo mass cutoff. This is why the *rms* peculiar velocities of the  $\Omega_m=0.25$  haloes *for a high mass cutoff* were comparable or in excess of those for larger values of  $\Omega_m$  even at higher redshifts. The very slight mass dependence (which seems statistically insignificant in Fig. 4) is exactly the issue when varying  $\Omega_m$ . It is clear that if we were to use an ever larger mass cutoff in that figure, the average *rms* velocity would *increase* while the number of haloes used decreased.

The anticorrelation in the parallel component is simply a result of infall, a non-linear process to which the linear theory is predictably blind. This behaviour was noted in Croft & Efstathiou (1995); in an effort to continue using linear predictions, the authors adjusted the smoothing length in the linear model and selected velocities below a cutoff. They conclude this approach introduces a strong bias in parameter determination. We examined this effect at different redshifts to determine how this discrepancy with linear theory has evolved. By redshift  $z=0.667$ , the few haloes massive enough to produce a Sunyaev–Zel’dovich effect are so rare as to have come from extremely overdense regions where collapse has been accelerated as if from a much higher  $\Omega_m$  universe. Consequently, infall is apparent out to large separations ( $\sim 40 h^{-1}$  Mpc). However, at lower redshifts where the rarity of such regions decreases, the anticorrelation scale and its overall (absolute) magnitude also decrease because the simulation is beginning to enter the era of dark energy domination (simply represented in our work by a cosmological constant). The extreme anticorrelation seen in Fig. 7 gives way to a much milder anticorrelation only seen at the smallest separations by  $z=0$ . Dark matter–cosmological constant equality occurs at  $z=0.44$ , 0.33 and 0.23 for  $\Omega_m=0.25$ , 0.3 and 0.35 respectively and marks the beginning of the end for new infall. Large modes which have not yet collapsed begin to decay during the acceleration phase, so volumes not undergoing gravitational collapse never will.

Fig. 5 demonstrates that the cosmological constant has become dominant more recently for the larger  $\Omega_m$  values because the parallel anticorrelation at  $r \sim 2.5 h^{-1}$  Mpc is still comparable (though negative) to about half the *rms* velocity. In contrast, for  $\Omega_m=0.25$ , the growth of structure at these comoving scales has already halted and the expansion has accelerated sufficiently to begin a decay towards linear theory values, especially for  $r \gtrsim 5 h^{-1}$  Mpc.

Finally, we remark on the history of particles destined to be in large mass haloes by  $z=0$ . The *rms* peculiar velocity derived from these sets of particles at  $z=19$  (Fig. 10) is lower than the linear theory prediction in agreement with the peak-background split prediction of Bardeen et al. (1986). In addition, the perpendicular and parallel components for separations  $r \lesssim 40 h^{-1}$  Mpc are also lower in amplitude than linear theory predictions. However, as the haloes assemble in the hierarchical paradigm (Figs. 8 and 9), the *rms* peculiar velocity surpasses linear theory and the perpendicular components (from  $2 \lesssim r \lesssim 40 h^{-1}$  Mpc) evolve towards linear theory values. The perpendicular component represents pairs of haloes responding only to some third large-scale fluctuation. It therefore probes the field more effectively than

the parallel component in which the pairs’ self-attraction at these scales dominates (on average) over gravitational attractions from other potential wells. Consequently, the perpendicular component gradually recovers the behaviour predicted by linear theory, modulo an overall boost in amplitude created by the mass selection bias mentioned above. In contrast, the parallel component gradually reflects the ever more common large scale infall until matter domination ends. The effect is heuristically like the function  $\Phi_{\parallel}$  mentioned in §2 above, though the scale occurs at smaller separation and the effect has a larger amplitude due to the non-linearity of the local density.

By  $z=0.25$ , when many of the  $z=0$  haloes have more than 60 particles within their virial radii, the parallel components begin to display the anticorrelation more apparent in Figs. 5–7. The coincidence in timing mentioned in §4.3.2 refers to the rarity of large scale potential wells compared to their amplitudes. As the largest mass haloes become more common, the infall felt by the ones still forming comes from more common smaller amplitude potential wells; consequently, there is less apparent infall in Fig. 9 than Fig. 7 simply because the volume probed by the particles destined for haloes is much larger than the rare, high-amplitude fluctuation dominated volume probed by fully formed high mass haloes.

## 6 CONCLUSIONS

The purpose of this work was two-fold. The primary goal was to examine how  $\Omega_m$  alone affects the velocity statistics of cluster-sized haloes using simulations as opposed to what linear theory predicts. The secondary purpose was to show that small ( $128^3$  particle) N-body simulations are sufficient to characterize the statistics of cluster-sized dark matter haloes and furthermore are fast enough to allow an exploration of parameter space in a reasonable amount of time.

We have shown that the dependence on  $\Omega_m$  for the *rms* peculiar velocity for a fixed value of  $\sigma_8$  and a fixed lower cutoff for the halo mass is counterintuitive to what linear theory predicts with a fixed  $\sigma_8$ . The peculiar velocities which develop for the largest mass haloes are faster for a smaller value of  $\Omega_m$  while the universe is matter dominated because the largest modes must have a greater amplitude for a fixed value of  $\sigma_8$ . However, since the decay of the (uncollapsed) largest modes occurs earlier for a smaller  $\Omega_m$ , there is a convergence towards an indistinguishable *rms* peculiar velocity at  $z \sim 0$  even though (in our work)  $\Omega_m$  varied by  $\sim 16$  per cent. Peculiar velocity catalogs from kinetic Sunyaev–Zel’dovich observations therefore have a much more complicated dependence on  $\Omega_m$  than other data from, e.g., the Cosmic Microwave Background, or large-scale galaxy redshift surveys.

In addition, we have shown that the two-point velocity functions (in real space) for cluster-sized dark matter haloes are as sensitive to these complicating biases as the *rms* peculiar velocity alone. The prospect of using the information from the two-point functions themselves to constrain  $\Omega_m$  are currently hindered by two major observational factors. First, the mass-based selection bias mentioned above affects the perpendicular component in a manner very similar to its effect on the *rms* velocity. Second, the sources of

noise mentioned in §1 are not guaranteed to be stochastic, yet are comparable in amplitude to the *rms* signal ( $\approx 200 \text{ km s}^{-1}$ ) (Knox et al., 2004; Nagai et al., 2003).

The full cosmological sensitivity of a kinetic Sunyaev-Zel'dovich derived peculiar velocity catalog has not been explored. This is where our secondary goal will come into play. Rough scaling shows the potential for a reasonable search through parameter space. For example, based on cluster statistics using multiple small ( $128^3$  particle) ART simulations on a current, fairly large supercomputer or multiple efficient clusters, we find:

$$T \sim \left( \frac{N_{\text{parameters}}}{5} \right) \left( \frac{N_{\text{values/parameter}}}{3} \right) \left( \frac{N_{\text{realizations/value}}}{10} \right) \left( \frac{8_{\text{CPU/realization}}}{N_{\text{CPUs}}} \right) 150 \text{ weeks.} \quad (26)$$

For instance, five parameters at three values each with ten realizations using only 160 CPUs would run in about two months. While the rest of Eq. (26) does scale linearly, the number of CPUs per realization is a non-linear function of the architecture of the computer and the performance of the simulation. The choice of  $8_{\text{CPU/realization}}$  is based on our simulations for this project and is only given as a guideline. Considering Moore's law, this an ever more conservative estimate. This is not on par with the speed of a Monte-Carlo Markov Chain method. However, when simulations are the only reliably accurate way to explore parameter space, a simpler Fisher Matrix type approach is now conceivable for multiple parameters.

## ACKNOWLEDGMENTS

AP would like to thank I. Zehavi, L. Knox, G. Efstathiou, N. Turok, A. Kravtsov and R. Sheth for useful conversations; in particular, AP would like to especially thank D. Nagai for his assistance in running simulations. AP is grateful for the anonymous referee's comments, which pointed out how to strengthen the final version of this paper. AP was supported at DAMTP by a PPARC rolling grant and at UC Davis by NASA GSRP Fellowship No. 1564 and NSF grant No. 0307961. The initial work in §3.4 was conducted on the IBM SP parallel computer 'Seaborg' at the National Research Scientific Computing Center in Berkeley, CA which is supported by the Office of Science of the Department of Energy under contract No. DE-AC03-76SF00098. The multiple-cosmology aspect of this work was finished using the UK National Cosmology Supercomputer in Cambridge, UK under a PPARC Rolling Grant.

## APPENDIX: TWO-POINT CORRELATIONS AT PEAKS

This appendix is provided primarily as a pedagogical tool. The nonlinear evolution of clusters and the mass selection effect of kSZ observations renders the consideration of peak vs. background statistics moot here, especially since, as shown below and in past papers, the peak statistics predict suppressed velocities compared to background, i.e., general field velocities. However, future methods of observation and

statistical analysis not mentioned in this paper may find the calculations presented below quite relevant.

We parallel the approach detailed in Bardeen et al. (1986) for calculating the peak statistics for a Gaussian distributed linear density field,  $\delta(\mathbf{x})$ . The density gradients at the peak,  $\eta_i(\mathbf{x}_p) = \nabla_i \delta|_{\mathbf{x}_p}$ , are zero (and nearly zero in some peak neighborhood) and the second derivatives of the density at the peak,  $\zeta_{ij}(\mathbf{x}_p) = \nabla_i \nabla_j \delta|_{\mathbf{x}_p}$ , form a  $3 \times 3$  symmetric matrix with positive eigenvalues. The six independent entries are relabelled  $\zeta_A$  where  $\{A = 1, 2, 3\}$  correspond to the diagonal elements (originally  $\zeta_{11}, \zeta_{22}$  and  $\zeta_{33}$ ) and  $\{A = 4, 5, 6\}$  correspond to the off-diagonals (originally  $\zeta_{23}, \zeta_{13}$  and  $\zeta_{12}$ ).

We shall adopt much of the notation found in Bardeen et al. (1986). We replace  $\zeta_1, \zeta_2, \zeta_3$ , with  $x, y, z$  where:

$$\begin{aligned} x &= -(\zeta_1 + \zeta_2 + \zeta_3)/\sigma_2 \\ y &= -(\zeta_1 - \zeta_3)/(2\sigma_2) \\ z &= -(\zeta_1 - 2\zeta_2 + \zeta_3)/(2\sigma_2) . \end{aligned} \quad (27)$$

Then,  $\delta$  correlates only with  $x$ , not  $y, z, \eta$ , nor  $\zeta_{4,5,6}$ . We also scale  $\delta$  by  $\sigma_0$ , and thus have constructed unitless variables with simple Gaussian widths:  $\langle v^2 \rangle = \delta^2/\sigma_0^2 = \langle x^2 \rangle = 15\langle y^2 \rangle = 5\langle z^2 \rangle = 1$ . In addition, if we ignore the velocities, we have a nearly symmetric auto-correlation matrix: the only non-zero, independent off-diagonal element is  $\langle vx \rangle = \sigma_1^2/(\sigma_0^2 \sigma_2^2)$ .

Of course, we are also concerned with the velocities. In linear perturbation theory, the divergence of the velocity field is given by the time derivative of the density field (Eq. (1)). Therefore, each component  $v_i$  only correlates with  $\eta_i$ , and to estimate the peak *rms* velocity we only need to examine the  $6 \times 6$  element matrix:

$$M = \begin{pmatrix} \langle vv \rangle & \langle v\eta \rangle \\ \langle \eta v \rangle & \langle \eta\eta \rangle \end{pmatrix} = \frac{1}{3} \begin{pmatrix} \sigma_v^2 I_3 & \dot{D}\sigma_0^2 I_3 \\ \dot{D}\sigma_0^2 I_3 & \sigma_1^2 I_3 \end{pmatrix}. \quad (28)$$

( $I_3$  is simply the  $3 \times 3$  identity matrix). Inverting this matrix and looking at the quadratic form  $Q = \mathbf{d}^T M^{-1} \mathbf{d}/2$  which appears in the Gaussian pdf  $P \propto e^{-Q}$  ( $\mathbf{d} = [v_i, \eta_i]$ ), while imposing the condition that  $\eta(\mathbf{x}_p) = 0$  leads to the expression given in Eq. (10) above for the autocorrelations of *peak* velocities.

Complicating matters, however, is the fact that many of the corresponding two-point correlations are not zero. One must reexamine the entire correlation matrix to see the effects on the peak velocity two-point functions (or, in fact, any other two-point functions). The list of relevant variables is now  $\mathbf{d} = [\delta_1, \mathbf{v}_1, \boldsymbol{\eta}_1, x_1, z_1, \zeta_{1A}, \delta_2, \mathbf{v}_2, \boldsymbol{\eta}_2, x_2, y_2, z_2, \zeta_{2A}; A = 4, 5, 6]$ , where the subscripts  $\{1, 2\}$  refer to the points  $\mathbf{x}$  and  $\mathbf{x} + \mathbf{r}$ , respectively. Our correlation matrix has now blossomed to  $26 \times 26$  elements<sup>1</sup>.

If we continue to follow Bardeen et al. (1986), the next step would be to rotate  $\zeta$  onto its principle axes. However, we cannot rotate both  $\zeta_1$  and  $\zeta_2$  simultaneously. Instead, it makes more sense to rotate the  $\hat{\mathbf{z}}$  axis to be in alignment

<sup>1</sup> "Even for the two-point function, the task of integrating over all these variables is not pleasant to contemplate." (Bardeen et al., 1986)

with the line-of-sight between the two points, i.e., along  $\mathbf{r}$ . This is what is done in evaluating Eq. (3).

The full analytic forms for the linear perturbation theory velocity correlation functions are often given as:

$$\begin{aligned}\Psi_{\perp}^{-1} &= \frac{\dot{D}_1 \dot{D}_2}{2\pi^2} \int dk |\delta_{k,0}|^2 \frac{j_1(kr)}{kr} W^2(kR) \\ &= \frac{\dot{D}_1 \dot{D}_2}{3} \int \frac{k^2 dk}{2\pi^2} \frac{|\delta_{k,0}|^2}{k^2} [j_0(kr) + j_2(kr)] W^2(kR)\end{aligned}\quad (29)$$

and:

$$\begin{aligned}\Psi_{\parallel}^{-1} &= \frac{\dot{D}_1 \dot{D}_2}{2\pi^2} \int dk |\delta_{k,0}|^2 [j_0(kr) - 2j_1(kr)/kr] W^2(kR) \\ &= \frac{\dot{D}_1 \dot{D}_2}{3} \int \frac{k^2 dk}{2\pi^2} \frac{|\delta_{k,0}|^2}{k^2} [j_0(kr) - 2j_2(kr)] W^2(kR)\end{aligned}\quad (30)$$

where we have explicitly added a  $-1$  superscript: in general, both the parallel and perpendicular  $\Psi^n$ 's will be defined as above, with a  $k^{2n}$  in the integral, much like the role of the  $n$  subscript for Eq. (11). We also define:

$$\phi_m^n(r) = D_1 D_2 \int \frac{k^2 dk}{2\pi^2} |\delta_{k,0}|^2 j_m(kr) k^n W^2(kR). \quad (31)$$

Below, we will implicitly assume that all  $\Psi$ ,  $\phi$  and  $\sigma$  functions are in terms of growth functions, not their time derivatives; thus we will use appropriate factors of  $\beta = \dot{D}/D$  whenever velocities appear.

The second lines in Eqs. (29) and (30) make it clear that we can rewrite  $\Psi_{\perp}^n$  above as  $\beta_1 \beta_2 (\phi_0^{2n} + \phi_2^{2n})/3$  and similarly  $\Psi_{\parallel}^n = \beta_1 \beta_2 (\phi_0^{2n} - 2\phi_2^{2n})/3$ . Also note that  $\xi(r) = \phi_0^0(r)$  and  $\sigma_0^2 = \phi_0^{2n}(0)$ . In this way, all the auto- and two-point correlations are expressible as linear combinations of the set of functions  $\phi_m^n(r)$ . As mentioned above, we will always rotate the  $z$ -axis to be parallel to  $\hat{\mathbf{r}}$ .

We solve for and list the various auto- and two-point correlations below, with subscript  $a = 1, 2$  for the two points  $\mathbf{x}$  and  $\mathbf{x} + \mathbf{r}$  respectively. For clarity, we also label the Kronecker-delta function with a superscript  $K$ . For completeness, the auto-correlations are repeated here:

$$\begin{aligned}\langle \nu_a \nu_a \rangle &= 1 \\ \langle v_{ai} v_{aj} \rangle &= \delta_{ij}^K \beta_a \sigma_{-1}^2 / 3 \\ \langle v_{ai} \eta_{aj} \rangle &= \delta_{ij}^K \beta_a \sigma_0^2 / 3 \\ \langle \eta_{ai} \eta_{aj} \rangle &= \delta_{ij}^K \sigma_1^2 / 3 \\ \langle \nu_a x_a \rangle &= \sigma_1^2 / (\sigma_0 \sigma_2) \\ \langle x_a x_a \rangle &= 1; \langle y_a y_a \rangle = 1/15; \langle z_a z_a \rangle = 1/5 \\ \langle \zeta_{ai} \zeta_{aj} \rangle &= \delta_{ij}^K \sigma_2^2 / 15 \\ &\quad \{i, j = 4, 5, 6\}\end{aligned}$$

all others being zero. For the following, we suppress the  $r$  argument as given, and rotate  $\hat{\mathbf{z}} \parallel \hat{\mathbf{r}}$ . The two-point correlations are:

$$\begin{aligned}\langle \nu_1 \nu_2 \rangle &= \phi_0^0 / \sigma_0^2 \\ \langle \nu_1 v_{2i} \rangle &= -\delta_{i3}^K \beta_2 \phi_1^{-1} / \sigma_0 \\ \langle \nu_2 v_{1i} \rangle &= \delta_{i3}^K \beta_1 \phi_1^{-1} / \sigma_0 \\ \langle \nu_1 \eta_{2i} \rangle &= -\delta_{i3}^K \phi_1^1 / \sigma_0 = -\langle \nu_2 \eta_{1i} \rangle \\ \langle \nu_1 x_2 \rangle &= \phi_0^2 / (\sigma_0 \sigma_2) \\ \langle \nu_1 y_2 \rangle &= \phi_2^2 / (2\sigma_0 \sigma_2) \\ \langle \nu_1 z_2 \rangle &= -\phi_2^2 / (2\sigma_0 \sigma_2) \\ \langle \nu_1 \zeta_{2i} \rangle &= 0; \quad \{i = 4, 5, 6\}\end{aligned}\quad (32)$$

$$\begin{aligned}\langle \mathbf{v}_1 \mathbf{v}_2 \rangle &= \beta_1 \beta_2 [\Psi_{\perp}^{-1} \mathbf{I} + (\Psi_{\parallel}^{-1} - \Psi_{\perp}^{-1}) \hat{\mathbf{r}} \hat{\mathbf{r}}] \\ \langle \mathbf{v}_1 \boldsymbol{\eta}_2 \rangle &= \beta_1 [\Psi_{\perp}^0 \mathbf{I} + (\Psi_{\parallel}^0 - \Psi_{\perp}^0) \hat{\mathbf{r}} \hat{\mathbf{r}}] \\ \langle \mathbf{v}_2 \boldsymbol{\eta}_1 \rangle &= \beta_2 [\Psi_{\perp}^0 \mathbf{I} + (\Psi_{\parallel}^0 - \Psi_{\perp}^0) \hat{\mathbf{r}} \hat{\mathbf{r}}]\end{aligned}\quad (33)$$

$$\begin{aligned}\langle v_{1i} x_2 \rangle &= -\delta_{i3}^K \beta_1 \phi_1^1 / \sigma_2 \\ \langle v_{1i} y_2 \rangle &= \delta_{i3}^K \beta_1 (\phi_1^1 / 5 - 3\phi_3^1 / 10) / \sigma_2 \\ \langle v_{1i} z_2 \rangle &= -\langle v_{1i} y_2 \rangle \\ \langle v_{1i} \zeta_{2j} \rangle &= \beta_1 (\phi_1^1 + \phi_3^1) (\delta_{i2}^K \delta_{j4}^K + \delta_{i1}^K \delta_{j5}^K) / 5 \quad \{j = 4, 5, 6\} \\ \langle \boldsymbol{\eta}_1 \boldsymbol{\eta}_2 \rangle &= [\Psi_{\perp}^1 \hat{\mathbf{I}} + (\Psi_{\parallel}^1 - \Psi_{\perp}^1) \hat{\mathbf{r}} \hat{\mathbf{r}}] \\ \langle \eta_{1i} x_2 \rangle &= -\delta_{i3}^K \phi_1^3 / \sigma_2 = -\langle \eta_{2i} x_1 \rangle \\ \langle \eta_{1i} y_2 \rangle &= \delta_{i3}^K (\phi_1^3 / 5 - 3\phi_3^3 / 10) / \sigma_2 = -\langle \eta_{2i} y_1 \rangle \\ \langle \eta_{1i} z_2 \rangle &= -\langle \eta_{1i} y_2 \rangle = -\langle \eta_{2i} z_1 \rangle \\ \langle \eta_{1i} \zeta_{2j} \rangle &= (\phi_1^3 + \phi_3^3) (\delta_{i2}^K \delta_{j4}^K + \delta_{i1}^K \delta_{j5}^K) / 5 \quad \{j = 4, 5, 6\} \\ \langle x_1 x_2 \rangle &= \phi_0^4 / \sigma_2^2 \\ \langle x_1 y_2 \rangle &= \phi_2^4 / (2\sigma_2^2) = -\langle x_1 z_2 \rangle \\ \langle y_1 y_2 \rangle &= [19\phi_4^4 / 140 - \phi_2^4 / 21 + \phi_0^4 / 15] / \sigma_2^2 \\ \langle y_1 z_2 \rangle &= (\phi_2^4 / 7 - 3\phi_4^4 / 28) / \sigma_2^2 \\ \langle z_1 z_2 \rangle &= [27\phi_4^4 / 140 + \phi_2^4 / 7 + \phi_0^4 / 5] / \sigma_2^2 \\ \langle \zeta_{14} \zeta_{24} \rangle &= [-4\phi_4^4 / 35 - \phi_2^4 / 21 + \phi_0^4 / 15] / \sigma_2^2 \\ &= \langle \zeta_{15} \zeta_{25} \rangle \\ \langle \zeta_{16} \zeta_{26} \rangle &= [\phi_4^4 / 35 + 2\phi_2^4 / 21 + \phi_0^4 / 15] / \sigma_2^2\end{aligned}\quad (34)$$

Note that most of the correlations are the same under  $\mathbf{r} \rightarrow -\mathbf{r}$  except those involving one  $\boldsymbol{\eta}$  or one  $\mathbf{v}$  which pick up a minus sign e.g., Eqs. (32) and (34); and those involving only one  $\mathbf{v}$  which forces  $D_1 \rightarrow D_2$  and  $\dot{D}_2 \rightarrow \dot{D}_1$ , e.g., Eqs. (32) and (33). In the limit where we ignore correlations at distances large enough to reflect a significant difference between  $D_1$  and  $D_2$  or between their time derivatives, this becomes a nitpicking concern.

To understand peak velocity two-point correlations, we must now perform the following steps. First, we construct the required  $26 \times 26$  matrix  $M$  using the above results and invert it. Next, we integrate the probability distribution given by  $P \propto e^{-Q}$  where  $Q = \mathbf{d}^T M^{-1} \mathbf{d} / 2$  over all the variables except the velocities: over  $\nu_1$  and  $\nu_2$  from the peak cutoff (such as  $\approx 3$ ) to infinity; and over all values of the second derivative which meet the positive eigenvalue criterion mentioned above. Third, we set the density derivatives  $\eta_{ai}$  equal to zero. The last step is to read off the remainder of the correlation matrix for the velocities, much like what was done to derive Eq. (10) above.

## REFERENCES

Bahcall N. A., Oh S. P., 1996, Bulletin of the American Astronomical Society, 28, 1428  
 Bardeen J. M., Bond J. R., Kaiser N., Szalay A. S., 1986, ApJ, 304, 15  
 Bertschinger E., Gelb J. M., 1991, Computers in Physics, 5, 164  
 Bridle S. L., Zehavi I., Dekel A., Lahav O., Hobson M. P., Lasenby A. N., 2001, MNRAS, 321, 333  
 Carlstrom J. E., Holder G. P., Reese E. D., 2002, ARA&A, 40, 643

Colberg J. M., White S. D. M., MacFarland T. J., Jenkins A., Pearce F. R., Frenk C. S., Thomas P. A., Couchman H. M. P., 2000, MNRAS, 313, 229

Croft R., Efstathiou G., 1995, in Proceedings of the 11th Potsdam Cosmology Workshop: *Large Scale Structure in the Universe*, ed. Mücke, J. P. , et al. , World Scientific, Constraints on the Power Spectrum of Mass Fluctuations from Galaxy Cluster Peculiar Velocities. pp 101–+

Efstathiou G., Davis M., White S. D. M., Frenk C. S., 1985, ApJS, 57, 241

Eisenstein D. J., Hüt P., 1998, ApJ, 498, 137

Feldman H., Juszkiewicz R., Ferreira P., Davis M., Gaztañaga E., Fry J., Jaffe A., Chambers S., da Costa L., Bernardi M., Giovanelli R., Haynes M., Wegner G., 2003, ApJ, 596, L131

Gorski K., 1988, ApJ, 332, L7

Hamana T., Kayo I., Yoshida N., Suto Y., Jing Y. P., 2003, MNRAS, 343, 1312

Holder G., Haiman Z. , Mohr J. J., 2001, ApJ, 560, L111

Holder G. P., 2004, ApJ, 602, 18

Jacoby G. H., Branch D., Clardullo R., Davies R. L., Harris W. E., Pierce M. J., Pritchett C. J., Tonry J. L., Welch D. L., 1992, PASP, 104, 599

Jenkins A., Frenk C. S., White S. D. M., Colberg J. M., Cole S., Evrard A. E., Couchman H. M. P., Yoshida N., 2001, MNRAS, 321, 372

Juszkiewicz R., Springel V., Durrer R., 1999, ApJ, 518, L25

Knox L., Holder G. P., Church S. E., 2004, ApJ, 612, 96

Kravtsov A. V., 1999, Ph.D. Thesis

Ma C., Fry J. N., 2002, Physical Review Letters, 88, 211301

Mo H. J., White S. D. M., 1996, MNRAS, 282, 347

Nagai D., Kravtsov A. V., Kosowsky A., 2003, ApJ, 587, 524

Peel A., Knox L., 2002, in Proceedings of the 5th International UCLA Symposium: *Sources and Detection of Dark Matter and Dark Energy in the Universe*, Nucl. Phys. B Proc. Suppl., 124, Using Galaxy Cluster Peculiar Velocities to Constrain Cosmological Parameters. p. 83

Seljak U., Makarov A., Hirata C., Padmanabhan N., McDonald P., Blanton M., Tegmark M., Bahcall N., Brinkmann J., 2004, submitted to Phys. Rev. D

Seljak U., Warren M. S., 2004, MNRAS, 355, 129

Sheth R. K., Diaferio A., 2001, MNRAS, 322, 901

Sheth R. K., Tormen G., 1999, MNRAS, 308, 119

Strauss M. A., Willick J. A., 1995, Phys. Rep., 261, 271